UCRL-TR-219486

LAWRENCE
LIVERMORE
NATIONAL
LABORATORY

Ultrafast Radiation Detection by Modulation of an Optical Probe Beam

S.P. Vernon, M.E.Lowry

March 2, 2006

Disclaimer

Auspices Statement

This work was performed under the auspices of the U. S. Department of Energy (DOE) by the University of California, Lawrence Livermore National Laboratory (LLNL) under Contract No. W-7405-Eng-48. The project (03-ERD-007) was funded by the Laboratory Directed Research and Development Program at LLNL.

FY05 LDRD Final Report
Ultrafast Radiation Detection by Modulation of an Optical Probe Beam
LDRD Project Tracking Code: 03-ERD-007
Mark Lowry, Principal Investigator

Abstract
We describe a new class of radiation sensor that utilizes optical interferometry to measure radiation-induced changes in the optical refractive index of a semiconductor sensor medium. Radiation absorption in the sensor material produces a transient, non-equilibrium, electron-hole pair distribution that locally modifies the complex, optical refractive index of the sensor medium. Changes in the real (imaginary) part of the local refractive index produce a differential phase shift (absorption) of an optical probe used to interrogate the sensor material. In contrast to conventional radiation detectors where signal levels are proportional to the incident energy, signal levels in these optical sensors are proportional to the incident radiation energy flux. This allows for reduction of the sensor form factor with no degradation in detection sensitivity. Furthermore, since the radiation induced, non-equilibrium electron-hole pair distribution is effectively measured "in place" there is no requirement to spatially separate and collect the generated charges; consequently, the sensor risetime is of the order of the hot-electron thermalization time ≤ 10 fs and the duration of the index perturbation is determined by the carrier recombination time which is of order ~ 600 fs in, direct-bandgap semiconductors, with a high density of recombination defects; consequently, the optical sensors can be engineered with sub-ps temporal response. A series of detectors were designed, and incorporated into Mach Zehnder and Fabry-Perot interferometer-based detection systems: proof of concept, lower detection sensitivity, Mach-Zehnder detectors were characterized at beamline 6.3 at SSRL; three generations of high sensitivity single element and imaging Fabry-Perot detectors were measured at the LLNL Europa facility. Our results indicate that this technology can be used to provide xray detectors and xray imaging systems with single xray sensitivity and S/N ~ 30 at xray energies ~ 10 keV.

Introduction/Background
The primary goal of this project was to develop prototype, high sensitivity, high-bandwidth, EMP immune, xray detector architectures to enable significant enhancement of the xray diagnostic capability for HEDP and ICF experiments at the National Ignition Facility (NIF). The concept for this new class of radiation detector is based on a novel radiation detection approach that employs an optical probe beam to sense radiation-induced changes in the optical refractive index of a sensor medium. This approach is founded on phenomena, and devices, that first emerged in studies of all-optical switching[1].

Of particular import are processes where one optical beam modulates (switches) a second optical beam, traversing the same medium, via a non-linear interaction; these processes are of interest as they enable new classes of devices, such as all-optical logic elements, for high-speed optical networking technologies. One important mechanism utilizes optical absorption of a first (pump) beam to generate

an e-h pair distribution in a semiconductor material. The e-h pairs produce a differential change in the refractive index of the semiconductor that, in turn, modulates the transmission of a second (probe) beam; the presence (or absence) of the pump beam can be used to "switch" the optical probe beam. This interaction can be used to implement the basic logical building blocks required for optical computing and optical networking.

The interaction of ionizing radiation with a semiconductor medium also produces a transient, non-equilibrium, e-h pair distribution that results in a transient differential change in the local refractive index of the semiconductor. A probe beam traversing the semiconductor will be modulated by the radiation-induced change in the local refractive index – this is the physical basis of this new class of radiation detector.

In effect the detector "down-converts" the radiation-induced effects to the optical domain. Down-conversion, in itself, is a rather old idea, and there are several radiation detection approaches that rely upon it including scintillation, luminescence, and γ Cherenkov effects. However, the present embodiment allows a high-degree of independent control over the properties of the probe beam including the intensity, collimation, polarization, center wavelength and spectral width. This permits detailed engineering of the optical system trading off performance characteristics such as S/N, sensitivity, dynamic range and temporal response, to design detectors optimized for specific applications. Furthermore, since the detector is sensitive to changes in the optical refractive index of the sensor medium, the radiation-induced charge distribution is effectively measured "in place". Consequently, the detector is inherently high bandwidth and free from limitations imposed by charge transport.

There are a number of processes whereby e-h pair generation gives rise to modification of the optical refractive index of a semiconductor material including free carrier absorption, bangap-shrinkage and exciton bleaching[2]. In optical pumping experiments at low carrier densities, exciton bleaching is believed to be the dominant effect[3,4]. The free carriers screen the Coulomb interactions, inhibiting formation of the bound exciton and bleaching the optical absorption[5]. The exciton bleaching mechanism saturates at a saturation carrier density, ρ_{sat}, at high pump intensity. We anticipate that exciton screening will be the dominant mechanism producing the refractive index change at low xray fluence.

Consequently, the xray absorption induced change in refractive index, δn, arising from this mechanism should exhibit (1) saturation behavior as the carrier density is increased and a (2) resonant enhancement at frequencies in the vicinity of the exciton absorption[4,5], i.e.

$$\delta n = CF(\rho)G(\lambda). \qquad 1.0$$

For clarity, we have separated the charge density and wavelength dependence of the refractive index into two functions.

$$F(\rho) = \frac{\rho / \rho_{sat}}{1 + \rho / \rho_{sat}} \qquad 1.1$$

contains the saturation behavior, and

$$G(\lambda) = \frac{\Gamma}{1+\Gamma^2} \quad \text{where } \Gamma = \frac{\lambda_{gap} - \lambda}{\delta\lambda} \qquad 1.2$$

accounts for resonant enhancement in the region of the exciton absorption with linewidth $\delta\lambda$, at wavelength $\sim \lambda_{gap}$. In equation 1.0, C is a constant of proportionality; for GaAs, C ~ 0.1, $\rho_{sat} \sim 10^{18}$, $\delta\lambda \sim 4$ nm.

In Fig.1 we consider a volume of semiconductor material subject to xray flux Φ_{xray}, with xray energy E_{xray}. The absorbed xrays induce local variations in the refractive index δn. For the purposes of this discussion, we ignore variations in the imaginary part of the complex refractive index; consequently, the index variations are phase objects.

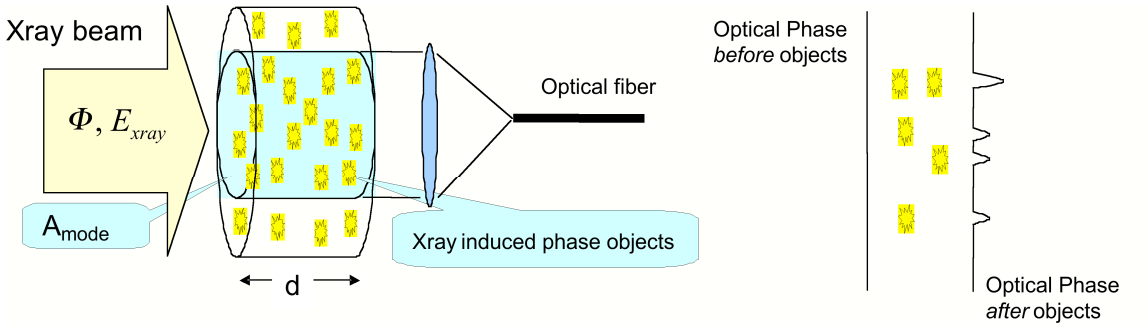

Figure1. Illustration of the phase disturbance of a collimated plane wave traversing a semiconductor material containing radiation induced refractive index variations (phase objects).

The sample is also irradiated with an optical beam of uniform intensity and cross sectional area A_{mode}, incident from a fiber collimator system. The right panel of the figure illustrates the spatial variation in the optical phase of the probe beam before and after traversing the sample. Note that those portions of the beam that encounter phase objects acquire a phase shift with respect to the unperturbed beam. We will approximate the phase objects as cubes of volume s_{rad}^3.

The phase shift acquired for an optical beam of wavelength λ traversing a phase object of size s_{rad}^3 is

$$\delta\varphi = \frac{2\pi}{\lambda} s_{rad} \delta n \qquad 1.3$$

where δn is given by Eq.1.0. In a mean field approximation, the average phase shift of the probe beam over the mode area is given by

$$\overline{\delta\varphi} = \frac{2\pi N_{xray} s_{rad}^3}{\lambda A_{Mode}} \delta n = \frac{2\pi p_{xray} \Phi_{xray} s_{rad}^3 \delta n}{\lambda} = \kappa(\lambda) p_{xray} \Phi_{xray} E_{xray} \qquad 1.4$$

Where

$$\kappa(\lambda) = \frac{2\pi C G(\lambda)}{\lambda \rho_{sat} E_{e-h}} \qquad 1.5$$

depends only on the semiconductor material properties. N_{xray} is the number of xrays absorbed within the sensor medium, Φ_{xray} is the incident xray flux and p_{xray} is the probability that the xray is absorbed within the sensor medium. In arriving at this result we have assumed that $\rho << \rho_{sat}$, $F(\rho) \approx \frac{\rho}{\rho_{sat}}$, and have used the identity $\rho s_{rad}^3 = \frac{E_{xray}}{E_{e-h}}$, e.g. the number of electron-hole pairs generated by absorption of a single xray is given by the ratio of the xray energy to the e-h pair formation energy.

Note that, provided that there are multiple xray absorption events within the sensor medium, i.e. $N_{xray} \geq 2$, the generated signal is independent of the sensor size and depends solely upon probe wavelength, sensor material properties and the incident energy flux. This stands in marked contrast to conventional xray detectors where signal levels are, characteristically, proportional to absorbed energy.

Research Activities
Our three-year research effort focused on demonstration of the viability of the detection concept in year one, improving sensor sensitivity in year two and extending the detection approach to xray imaging in year three.

Year 1: The native time structure of synchrotron radiation and the inherent sensitivity advantages afforded by signal averaging and phase-sensitive detection naturally led us to consider utilizing synchrotron sources for our proof of concept experiments. The high spectral brightness and native time structure of the SPEAR storage ring at the Stanford Synchrotron Radiation Laboratory made it a nearly ideal source for the initial experiments. Measurements were performed on beamline 6.3 using quasi-monochromatic x-radiation at 8.9 keV beam energy[6].

Proof of concept sensors were planar ridge waveguide structures with InP cladding and an $In_{1-x}Ga_xAs_yP_{1-y}$ core designed for probe wavelengths ~ 1550 nm. Operating at C-band, 1535-1565 nm, permitted us to use standard telecom hardware in the design and construction of the balanced-bridge, Mach-Zehnder interferometer detector illustrated in Figure 2. A narrow-band, broadly tunable source and Erbium doped fiber amplifier (EDFA) were use to provide a high-power low-noise optical probe. The polarization controller P, matched the launched polarization to the linearly polarized eigen states of the polarization preserving optical fiber used in the remainder of the system. Feedback for the polarization controller was derived from a stand-alone optical detector not shown in the figure located upstream of the fiber splitter. The waveguide sensor was placed in one arm of the interferometer. The reference leg contained both amplitude and phase adjustments used to balance and lock the interferometer, via computer control, to the ½ power point of the system response function (here small deviations in signal amplitude are approximately linear). The four-port 50:50 directional coupler combines the signals from the sample and reference arms of the interferometer; signals are available at two detector channel outputs. Note that in this arrangement, signals arising from xray

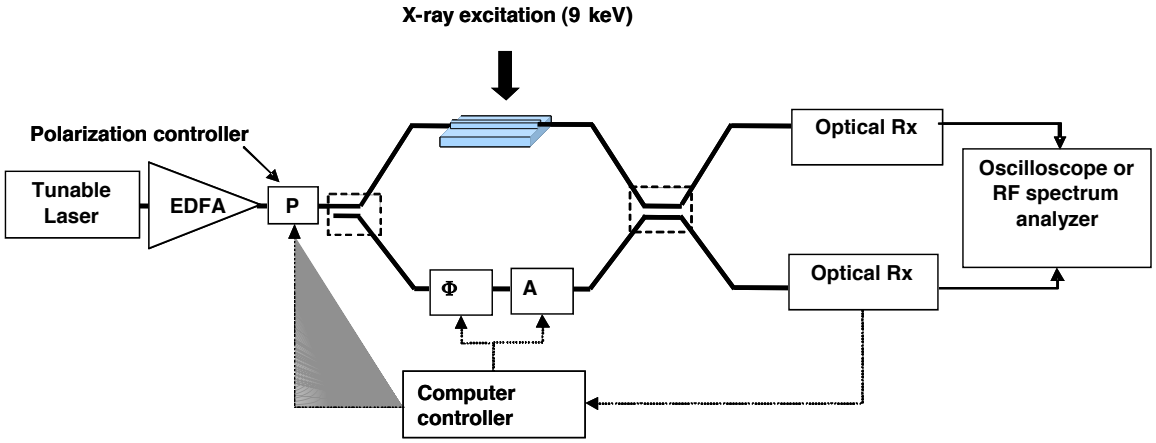

Figure 2. Diagram of the balanced-bridge Mach-Zehnder interferometer fielded at SSRL. The objects in the dashed boxes are polarization maintaining, optical fiber, directional couplers.

induced optical absorption in the sensor are symmetrically propagated to the two outputs; signals arising from differential phase shifts (xray induced variation in the real part of the refractive index of the sensor) are complementary. The fiber-pigtailed sensor element is shown in Figure 3.

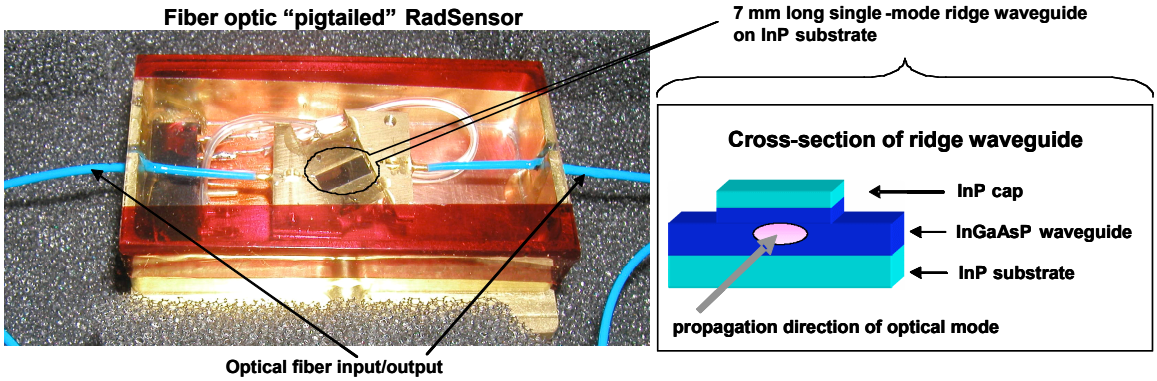

Figure 3. Photograph (left) of the fiber-pigtailed sensor package used in the SSRL experiments and a schematic (right) cross section of the rigde waveguide.

The time structure of the synchrotron radiation pattern is periodic. For these experiments, the ring was operated in dedicated mode with a single bucket fill, i.e. a single packet of electrons orbited the ring with a period of 781 nsec. The time structure of the xray signal characteristic of the single bucket fill pattern, as measured with a diamond PCD, is illustrated in Figure 4. Figure 5 shows the typical response of the Mach-Zehnder interferometer outputs measured during exposure of a sensor to the single bucket radiation pattern. The two panels correspond to signals measured at the two outputs. The signals are complementary indicating that xray induced changes in the real-part of the sensor refractive index (phase shifts) dominate the sensor response. Closer inspection reveals that the interferometer exhibits fast risetime and a slower decay time. Interestingly, the signals nearly

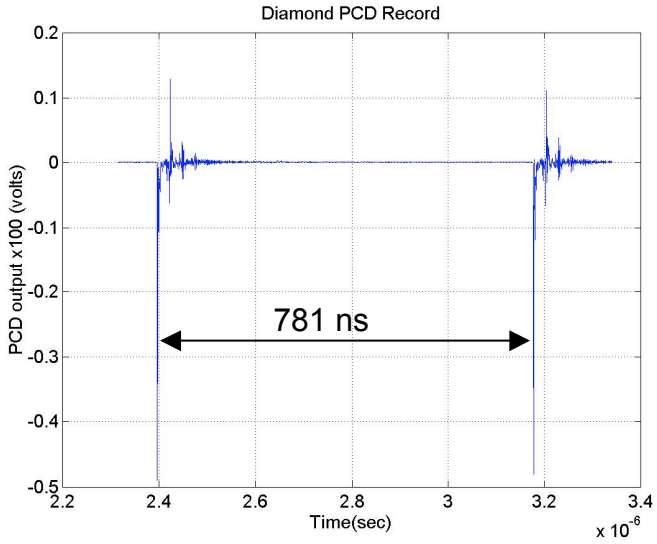

Figure 4. Temporal dependence of the xray radiation during a single bucket fill as measured with a diamond PCD detector.

return to the baseline before the next pulse occurs, implying that the sensor has nearly full recovered within the 781 nsec between pulses. The recovery is not complete however; there is a long-lived component to the decay that is not seen in the figure.

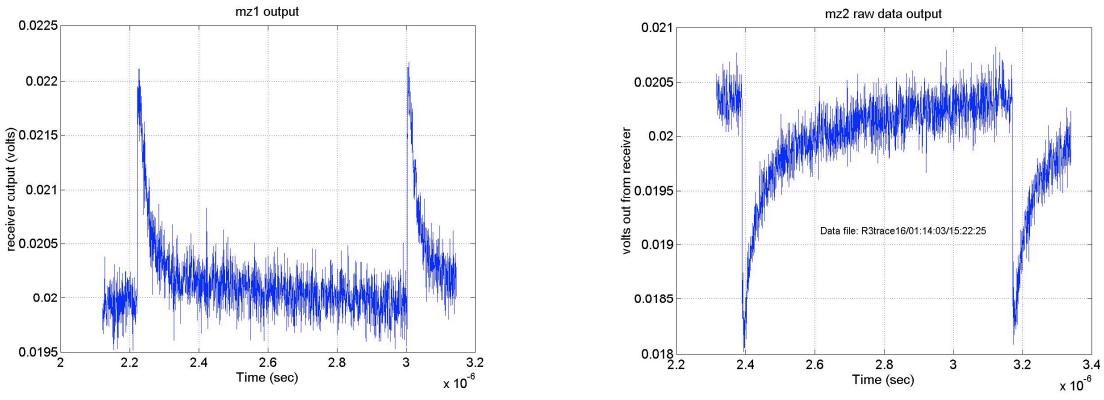

Figure 5. Typical sensor response to a single bucket fill pattern. The outputs are complementary indicated that the dominant effect of xray absorption is modification of the real-part of the sensor medium refractive index. The waveguide core was $In_{1-x}Ga_xAs_yP_{1-y}$ with x=0.215 and y = 0.542.

During the course of these experiments we repeatedly ramped the phase adjustment driving the interferometer over multiple fringes allowing us to establish voltage levels corresponding the fringe maximum and minimum. These values were used to

normalize the sensor voltage excursions and extract the radiation induced phase shifts. The detector sensitivity was derived by calculating the xray absorption in the waveguide core using the measured xray beam footprint, the spatially integrated incident xray flux incident upon the sensor (as measured with an ion chamber), the known ridge waveguide material compositions and known device dimensions. For $In_{1-x}Ga_xAs_yP_{1-y}$, with $0.2 \le x \le 0.4$, $0.54 \le y \le 0.73$, $\kappa \sim 4\times10^{-5}\,\frac{mrad-\mu m^2}{eV}$ in the spectral range near 1550 nm.

Year 2: With the successful demonstration of the Radoptic effect concluded in the first year, year two efforts were devoted to the development of radoptic sensors with useful single-transient response. The sensitivity of the detector is significantly enhanced via adoption of a Fabry-Perot architecture. This effectively increases the interaction between the probe and the sample. The light is "stored" and recycled within the Fabry-Perot cavity, repeatedly traversing the sensor volume and, repeatedly sampling the radiation induced index perturbation. Detection efficiency is increased by the cavity finesse f; however the increase in sensitivity requires simultaneous degradation in the temporal response.

In Figure 6 we illustrate the basic architecture of the Fabry-Perot sensor (left panel) and an illustration of the dependence of the device reflectance on the cavity round-trip phase shift, ϕ_{23}. Note that the xray induced transients in the refractive index

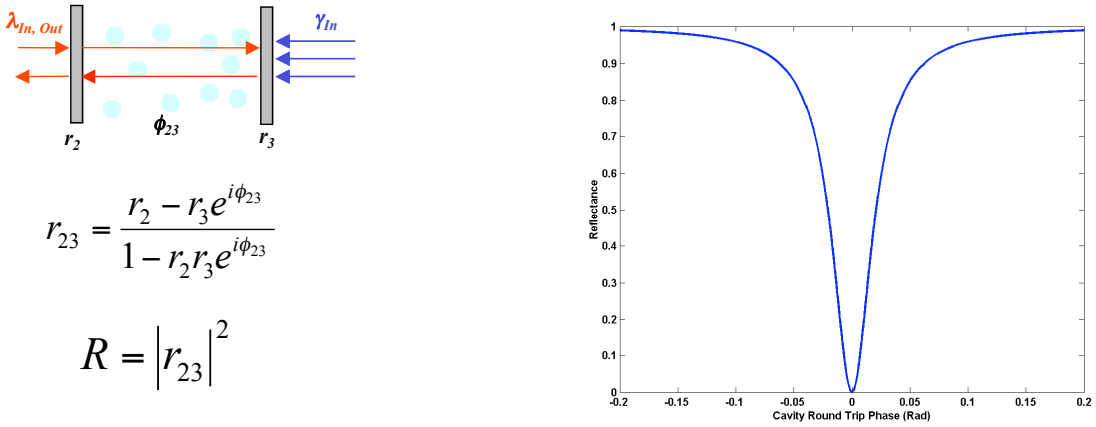

Figure 6. The Fabry-Perot sensor (left panel) is comprised of a semiconductor sensor medium surrounded by mirrors, of reflectance r_1 and r_2. The blue circles represent regions of the sensor where absorbed radiation has modified the sensor material refractive index. The dependence of the sensor reflectance, R, on the cavity round-trip phase shift, ϕ_{23}, for $f \sim 80$, $r_1 = r_2 \sim 0.92$, is illustrated in the (right panel).

of the sensor medium modify the cavity round-trip phase shift and therefore modulate the reflectance of the sensor. For small transients, the radiation induced signal level is set by the slope of the response curve at the operating point, i.e the slope is ~ 0 at the null and a maximum at R~0.3; consequently, both the sensitivity and the dynamic range of the sensor depend upon the selection of the quiescent operating point. We note that high-bandwidth, single transient recording applications admit AC coupling of the detection system; quiescent "background" signals arising from off-null operation do not contribute to the detected signal.

The baseline design for the preliminary Fabry-Perot sensor is illustrated in Figure 7.

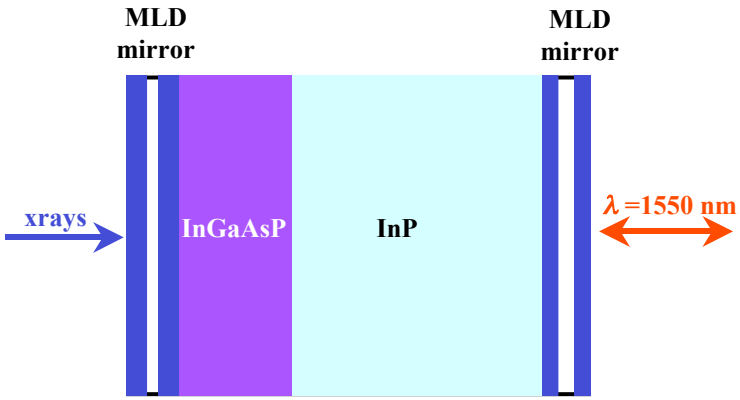

Figure 7. Schematic illustration of the baseline Fabry-Perot sensor design. The sensor consists of a 5 μm thick, $In_{1-x}Ga_xAs_yP_{1-y}$ epilayer on a InP wafer substrate, surrounded by broadband, high-reflectance, MLD mirrors.

The sensor consists of a 5 μm thick, $In_{1-x}Ga_xAs_yP_{1-y}$ epilayer, with a composition selected to produce a band-edge at 1475 nm, grown on a double side polished InP wafer substrate. The Fabry-Perot interferometer was formed by depositing broadband SiO_2/Ta_2O_5 MLD high reflectance mirrors on both sides of the wafer. The InP side was illuminated by the probe light beam, the $In_{1-x}Ga_xAs_yP_{1-y}$ side was exposed to the xray beam. The sensor was mounted in the housing illustrated in Figure 8 and coupled to a custom fiber GRIN lens collimator that illuminates the

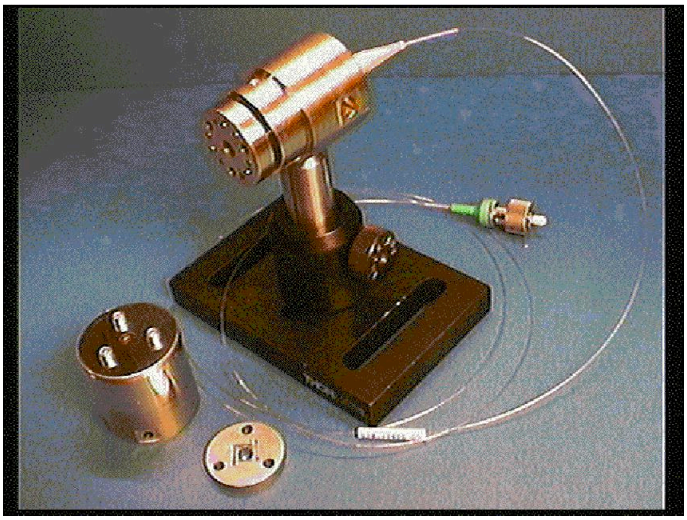

Figure 8. Exploded view of the sensor mounting system. The optical fiber assembly is a fiber GRIN lens collimator that illuminates the Fabry-Perot and collects the reflected illumination.

Fabry-Perot interferometer with collimated 1550 nm light and couples the reflected light into the detection system schematically illustrated in Figure 9.

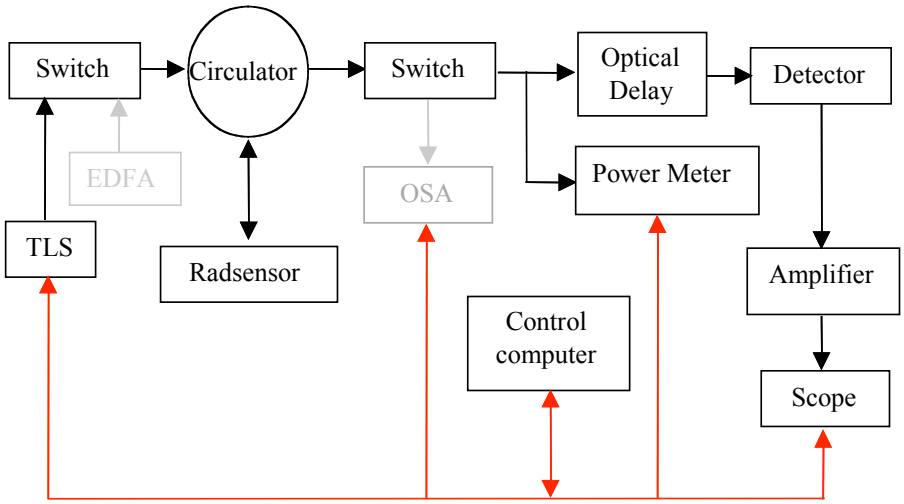

Figure 9. Schematic of the optical detection system employed with the Fabry-Perot sensors.

The optical detection system was fiber optics based and consisted of a tunable probe beam, an optional amplifier stage and a fiber optic circulator. Light reflected from the sensor was routed to the exit port of the circulator and passed through an optical delay line to a fast photodiode detector. The detector signal was amplified and recorded on a recording oscilloscope. An optical switch at the circulator output allowed redirection of the optical beam to an optical spectrum analyzer (OSA). The OSA detector was used to set the source wavelength to the desired operating point. A 90:10 fiber splitter and optical power meter allowed continuous measurement of probe beam power during the course of the experiment. Early versions of the detection system employed polarization control and polarization maintaining optics upstream of the sensor. Later versions utilized non-polarization maintaining components. In order to relate detector voltage to phase shift the TLS wavelength was scanned over the wavelength range of interest, AM modulating the laser output and recording the modulated signal amplitude. This permitted mapping of the detector voltage to the sensor phase shift at each operating wavelength.

Xray experiments were performed at LLNL's ultra-short pulse laser facility (USP) using the arrangement illustrated in Fgure 10. A 100 mJ, 100 fs pulse duration, 800 nm laser was focused on a 12 μm thick pure Cu foil located at the center of a vacuum chamber maintained at ~ 10^{-6} torr. PIN diodes, with 20 μm thick Cu foil filters, located in front and ~ 25 cm distant from the laser target monitored the emitted xray flux. An identically filtered xray flux was incident on the optical sensor located 5.6 mm behind the Cu foil target. The Cu filters were used to limit the spectral bandwidth of the transmitted xray flux emitted by the laser-produced plasma. 1550 nm probe light was fiber coupled into the vacuum enclosure via a fiber-optic vacuum feed through. The laser pulse ~ 10^{12} Watts generates significant EMI; consequently, the optical signals were routed through ~ 1km optical fiber delay line. This delayed arrival of the optical signal at the photodetector by ~ 5

microseconds relative to the laser pulse. PIN diode and sensor waveforms were recorded using ~ 3 Ghz bandwidth oscilloscopes.

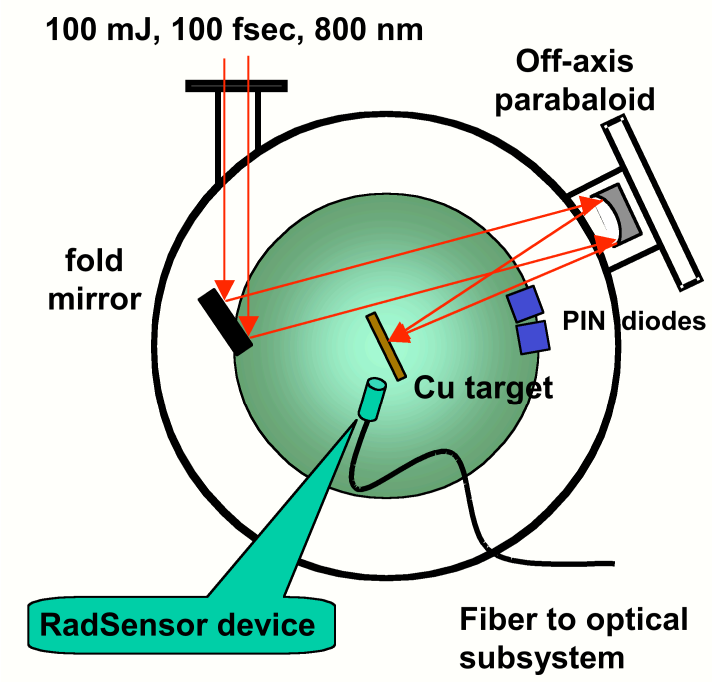

Figure 10. Schematic of the experimental arrangement employed in the single-transient sensor response measurements at LLNL's USP facility

In order to minimize technical risks associated with sensor fabrication, the baseline Fabry-Perot sensor architecture had both the $In_{1-x}Ga_xAs_yP_{1-y}$ sensor layer and the *InP* substrate within the resonant cavity (see Figure 7). This choice severely limited the optical performance of the sensor. Anti-parallelism of the substrate surfaces (wedge) cause walk-off of the probe beam, this severely degraded the finesse of the cavity and limited the reflectance of the sensor cavity. Most experiments required ~ 100 mW of probe power to obtain measurable reflected optical signals. This complicated the experiments. Residual optical absorption of the 100 mW probe beam induced sample heating and thermal expansion of the Fabry-Perot sensor during the experiments. These effects are illustrated in Figure 11, where we show OSA traces of the wavelength dependent cavity reflectivity measured over a sequence, ShotA-ShotH, of 8 high-power laser shots. First note that the wavelength dependent reflectivity of the sensor bares little resemblance to the theoretical predictions for a high finesse cavity and that there is ~3 fold variation in the amplitude of the reflectance variation as the wavelength is increased from 1545 – 1550 nm. Further note that the reflectance pattern systematically shifts to longer wavelengths as time elapses indicating a drift in the spectral response. In order to account for and track the drift an OSA scan was conducted prior to each high-power laser pulse. Note that for this sensor ~ 1 nm corresponds to a round-trip phase shift $\phi \sim 2\pi$.

In figure 12 we show the sensor response to a single high-power laser pulse. The laser-generated plasma produced an incident xray flux of ~ 60 Cu $K_\alpha/\mu m^2$ at the

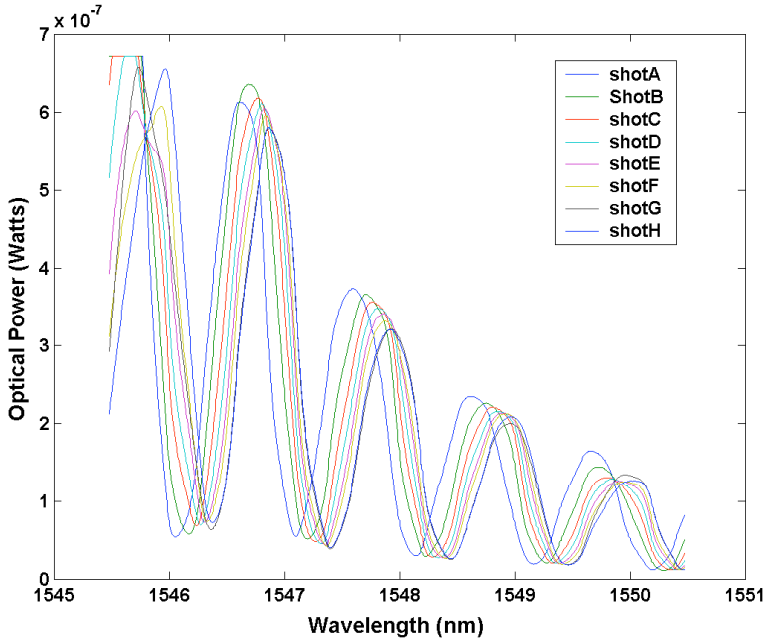

Figure 11. Wavelength dependent reflectivity of the sensor measured over a sequence of high-power laser shots. The drift is due to sample heating produced by optical absorption of the probe beam.

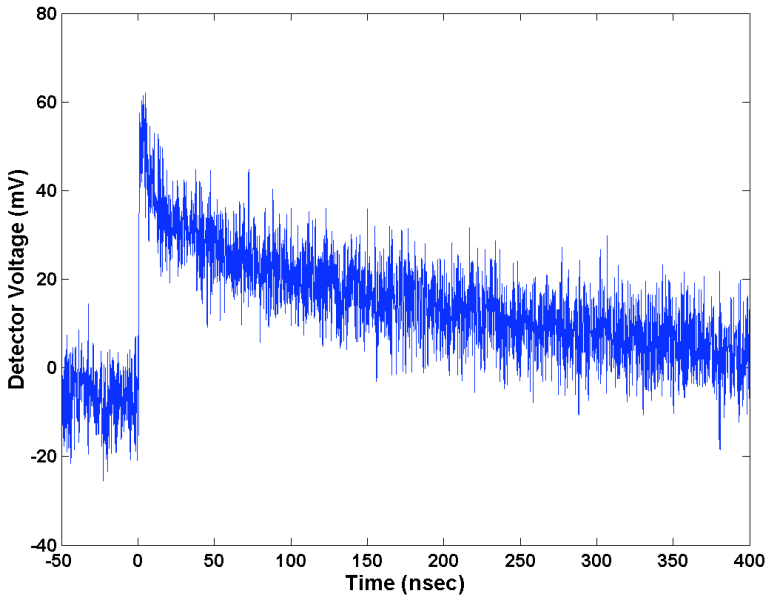

Figure 12. Single transient response of the Fabry-Perot sensor to x-radiation generated by laser ablation of a 12 μm thick Cu foil.

the sensor surface. The S/N ratio is ~ 5 with an instrument limited rise-time and a decay time of order 150 ns. Using the OSA data of Figure 11 we can relate the peak voltage excursion shown in Figure 12, to the peak sensor phase shift at the operating wavelength (or quiescent operating phase). This yields $\kappa(\lambda) = 1x10^{-4}\ \frac{mrad\text{ - }\mu m^2}{eV}$ at 1550 nm, which agrees, within a factor of two, with the value obtained from the earlier Mach-Zehnder experiments.

A modified sensor architecture, illustrated in Figure 13 below, was fabricated to circumvent problems associated with the earlier design. In this case the Fabry-

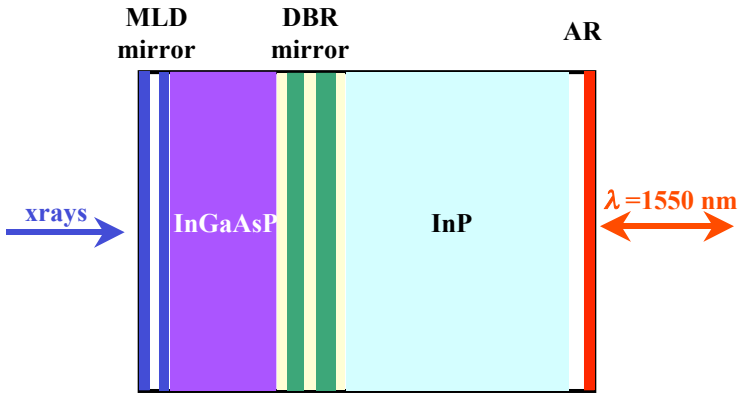

Figure 13. Improved design of the Fabry–Perot sensor. MLD and DBR mirrors surround the $In_{1-x}Ga_xAs_yP_{1-y}$ sensor layer. The sensor is illuminated through an AR coating applied on the rear surface of the InP wafer substrate.

Perot cavity was grown on the surface of the InP wafer. Initially, a high-reflectance $In_{1-x}Ga_xAs_yP_{1-y}/InP$ distributed Bragg reflector, DBR, (with a reflectance maximum at 1530 nm) was grown on a double side-polished InP substrate using MOCVD, and subsequently overcoated with a 5 μm of $In_{1-x}Ga_xAs_yP_{1-y}$. Magnetron sputter deposition techniques were used to deposit a high reflectance SiO_2/Ta_2O_5 MLD mirror, with a reflectance bandwidth similar to the DBR, on the $In_{1-x}Ga_xAs_yP_{1-y}$ layer, completing the Fabry-Perot cavity. Lastly a SiO_2/Ta_2O_5 antireflection coating was applied to the backside of the substrate to suppress unwanted reflections. Incident x-radiation passed through the MLD mirror and was partially absorbed in the $In_{1-x}Ga_xAs_yP_{1-y}$ sensor layer; the sensor was illuminated by a 1550 nm probe beam incident from the back surface of the substrate. Since the DBR and MLD were grown on the same side of the wafer, the parallelism between the mirror surfaces was significantly improved. The resultant Fabry-Perot cavities were truly superior with finesse approaching $f \sim 20$.

The cavities showed marked improvement in the wavelength dependent reflectance. A wavelength scan of a sensor is shown in Figure 14, where we plot cavity reflectance vs probe wavelength for a wavelength range spanning 10 nm. The blue curve is the measured response and the red curve is a best fit Lorentzian. The

reflectance null is at 1521 nm, with a FWHM of 2 nm. The improvement in the cavity design allowed us to reduce the input optical power by two orders of magnitude,

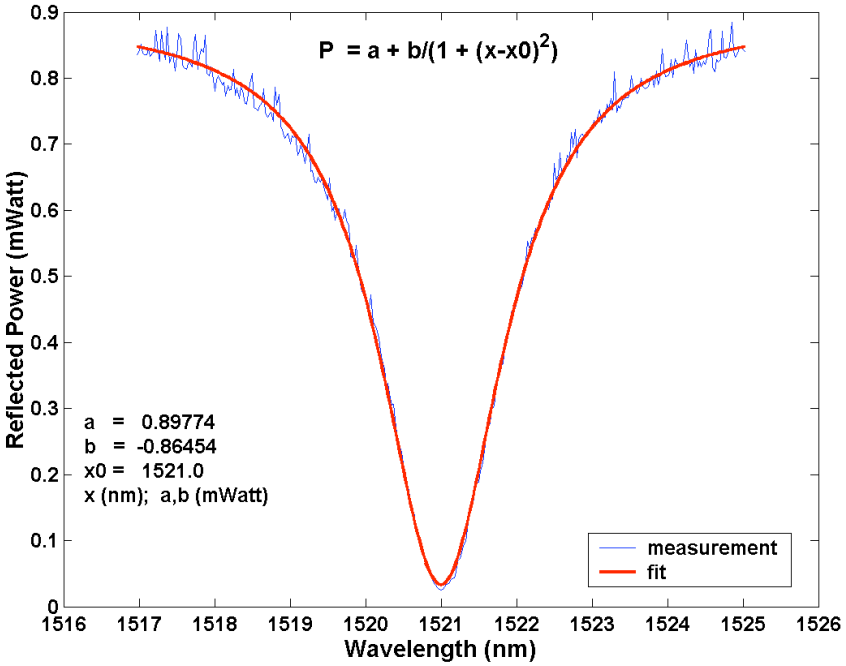

Figure 14. Wavelength dependent response of a typical second-generation Fabry-Perot sensor. The blue curve are the measured values, the red curve is the best-fit Lorentzian. Fitting parameters are given in the figure.

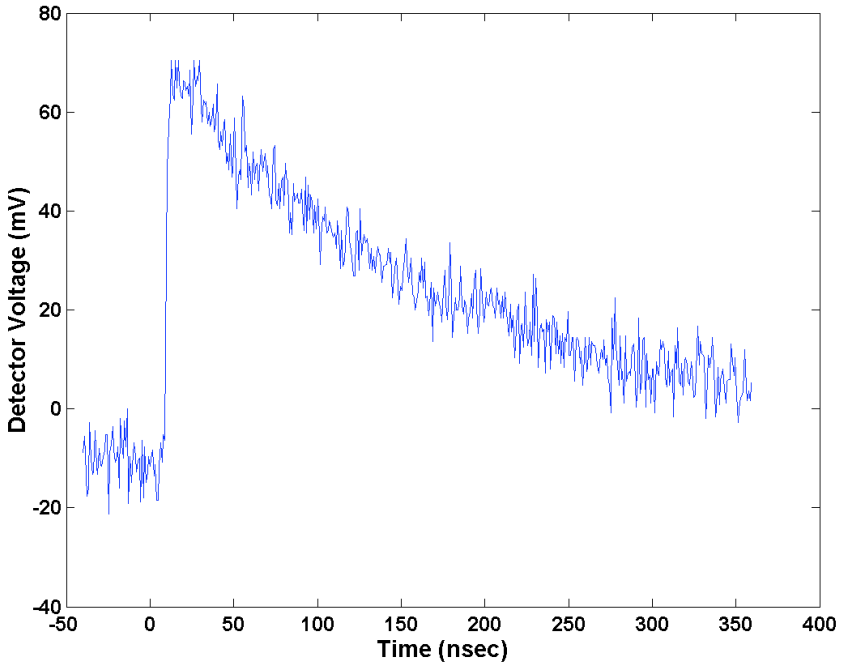

Figure 15. Single transient response of a second-generation Fabry-Perot sensor to x-radiation generated by laser ablation of a 12 μm thick Cu foil.

effectively eliminating problems associated with optical absorption induced drifts in the sensor response function. This led to marked improvement in the detection performance of the sensor as illustrated in Figure 15. The detected signal was obtained with an incident xray flux of ~ 20 Cu $K_\alpha/\mu m^2$ at the wafer surface and was measured with 1 mW of probe power. This represents a >300 fold improvement in in detection sensitivity over the first generation device. We estimate that the device would provide a a S/N ~2 at an xray flux 4 Cu $K_\alpha/\mu m^2$; consequently, a 1 μm^2 device with comparable response will have near single xray detection sensitivity. We find $\kappa(\lambda) = 2.5x10^{-4}\ \frac{mrad\text{ - }\mu m^2}{eV}$ at 1550 nm, a factor or 2.5 larger than the value derived for the first-generation sensor.

Year 3: With the viability of the detection approach validated and the experimental demonstration of near single xray detection sensitivity accomplished, year three was devoted to (1) a theoretical analysis of the viability this detection scheme for xray imaging and (2) experimental demonstration of xray imaging with radoptic detectors. A schematic design of a candidate imaging system is illustrated in Figure 16.

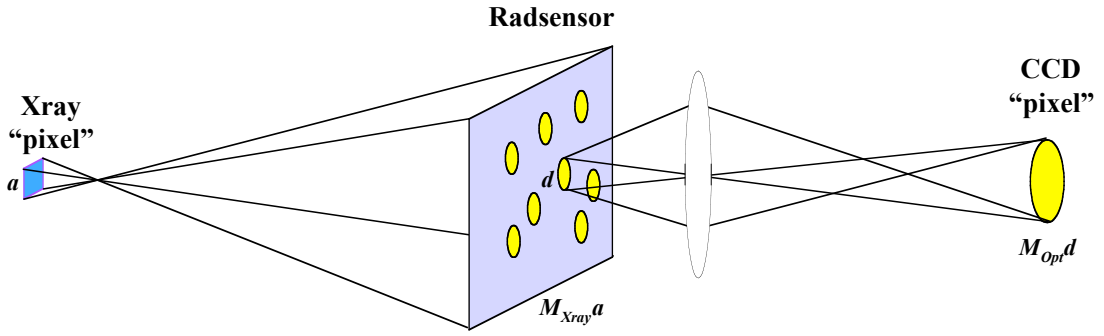

Figure 16. Schematic design of a Radoptic based xray imaging system incorporating xray and optical magnification. The yellow dots indicate a single xray event.

The resolution element in the object plane, the Xray "pixel" has a characteristic dimension, a. An xray optical system, with magnification M_{xray} relays an xray image of the object onto the Radoptic detector. The yellow dots in the figure indicate individual xray events (index disturbances) with characteristic dimension, d. An optical system with magnification M_{Opt} relays the optical image onto a recorder system (CCD). The low-flux limit corresponds to magnifications where there is, at most, a single xray event within a radoptic detector resolution element and/or a single CCD "pixel".

Figure 17 illustrates one implementation of the optical readout for a Radoptic detector used in xray imaging. A Pockels cell is used to gate a tunable laser

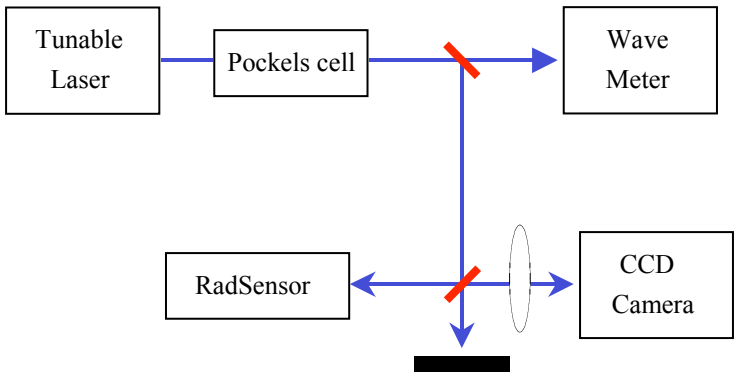

Figure 17. Schematic illustration of one embodiment of a radoptic xray imaging system. Beam splitters (red) are used to illuminate the sensing element and collect a a portion of the reflected beam with the optical recording system.

source and illuminate the radoptic sensor. A wavemeter is used to monitor the laser wavelength and match the laser wavelength to the Radsensor cavity. An optical imaging system relays radiation reflected from the radoptic detector onto a CCD camera. An xray source, not shown in the figure, irradiates the radoptic sensor synchronously with the laser pulse.

In the low flux limit, the xray flux for radoptic detector resolution elements containing xray events is inversely proportional the area of the resolution element area, i.e.

$$\Phi_{x-ray} = \frac{1}{A_{res}} \qquad 2.0$$

For Fabry-Perot sensors, resolution elements containing xray events will produce a phase shift, $\delta\phi$, of the reflected beam given by:

$$\delta\varphi = 2\kappa(\lambda)\Phi_{x-ray}E_{x-ray} = \frac{2\kappa(\lambda)E_{x-ray}}{A_{res}} \qquad 2.1$$

The factor of two represents the accumulated phase differential in a round-trip traversal of the cavity. Assuming that the index disturbance has a lifetime of t_{xray}, and that the radoptic detector is illuminated with P_0 photons/μm^2-sec, the number of photons reflected from the cavity, S_{x-ray}, due to the index perturbation is given by

$$S_{x-ray} = \left(P_0 A_{res}\frac{dR(\varphi)}{d\varphi}\delta\varphi\right)t_{x-ray} = 2P_0\kappa(\lambda)E_{x-ray}t_{x-ray}\frac{dR(\varphi)}{d\varphi} \qquad 2.2$$

The magnitude of the xray induced signal is independent of the dimension of the size of the xray resolution element.

If the reflected radiation is collected with a CCD camera, with gate width t_{gate}, the CCD will also record a background signal, B, due to the reflectance of the Fabry-Perot at the selected operating point, R_{Null}, which may be expressed as

$$B = P_0 A_{res} R_{Null} t_{gate} \qquad 2.3$$

Note that the background signal increases with the size of the resolution element.

The signal to noise ratio, for single-particle counting, can be expressed as

$$S/N = \frac{(QE)S_{x-ray}}{\sqrt{(QE)\left[S_{x-ray} + B\right] + N_{CCD}^2}}; \qquad 2.4$$

QE, is the quantum efficiency of the CCD, and N_{CCD}^2 is the CCD readout noise. Note that since B depends on the size of the resolution element the S/N ratio is area dependent.

In figure 18 we illustrate the predictions of Equation 2.4 for a Fabry-Perot imaging Radsensor as a function of cavity finesse for resolution elements between 3x3 and 6x6 μm. The simulations assume QE = 0.3, $t_{xray} = t_{gate}$ = 100 ns, N_{CCD} = 10 electrons,

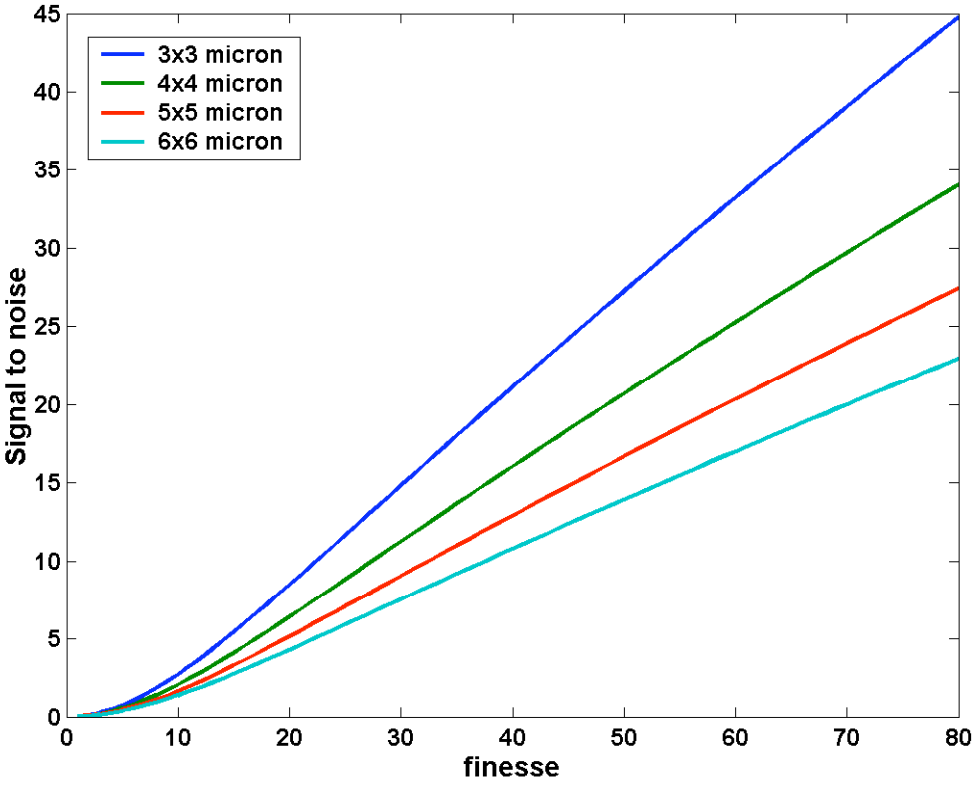

Figure 18. Predicted S/N ratio for Fabry-Perot sensors as a function of cavity finesse and size of the resolution element size. Parameters used in the simulations are described in the text.

an incident photon flux ~ 10^{15} photons/μm^2-sec and R_{Null} = 10^{-4}. The S/N model predicts that imaging can be performed with single xray sensitivity and a S/N ~ 30

for a single-particle, for resolution elements smaller than 5x5 μm for sensors with f ~ 80.

For the proof of concept demonstration we elected to use $GaAs$ as a sensor material and operate at wavelengths ~ 900 nm (above the $GaAs$ band-edge at 870 nm) – this would permit using conventional Si CCD cameras to record the optical image. The imaging sensor design is illustrated in Figure 19 and consisted of a 6.1 micron thick $GaAs$ layer surrounded by $GaAs/AlGaAs$ high reflectance DBR mirrors. The sensor

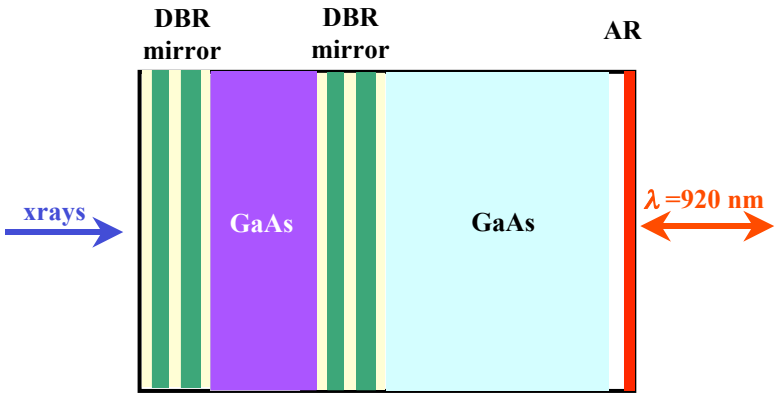

Figure 19. Schematic of the $GaAs$ based, 900 nm imaging RadSensor. Due to mismatch of the DBR mirrors the sensor was used in transmission mode.

layer and DBR mirrors were fabricated by a commercial vendor. At the outset, we intended to use the sensor in reflection mode and fabricated a SiO_2/Ta_2O_5 antireflection coating on the backside surface of the GaAs substrate. Mismatch in the reflectance bandwidth of the DBR mirrors required us to use the Fabry-Perot in transmission mode to yield low backgrounds and acceptable dynamic range. (Since the DBR mirrors are high reflectors, good extinction is observed, off-resonance, in transmission even when mirror reflectivities are slightly mismatched). This complicated the xray experiments since both the xray and optical probe beams had to illuminate the same side of the sensor. With this arrangement significant effort had to be devoted to appropriately shielding of the optical detection system from stray light generated during laser ablation of the Cu target.

A free space optical system was used to prepare a collimated, ~ 900 nm beam, irradiate the sensor, collect the transmitted radiation and relay a 1:1 image of the sensor surface onto a cooled CCD detector. The sample was oriented at 45 degrees with respect to both the 900 nm laser and the optical axis of the 800 nm drive laser used to generate the laser produced plasma. The layout of the optical system in the vacuum chamber is shown in Figures 20 and 21.

In order to calibrate the system the Cu foil target was removed, the 800 nm beam was attenuated and collimation optics were installed to produce a collimated 800 nm beam ~ 3mm in diameter which overlapped the 900 probe beam at the sensor surface. The pump energy is above the $GaAs$ bandgap; consequently, 800 nm

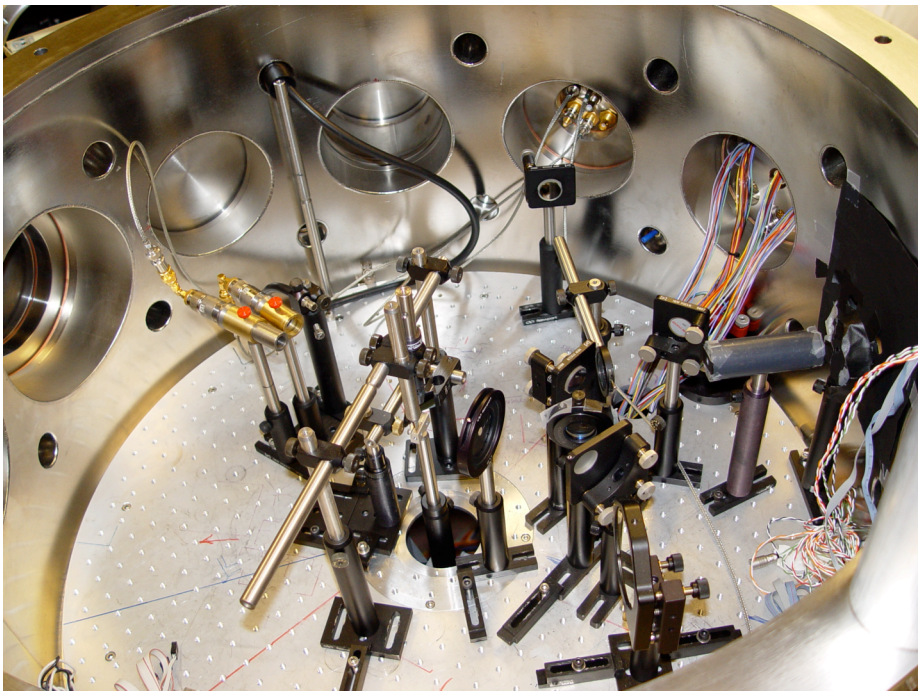

Figure 20. Top view of the experimental chamber. The brass housings hold Si PIN diode xray detectors.

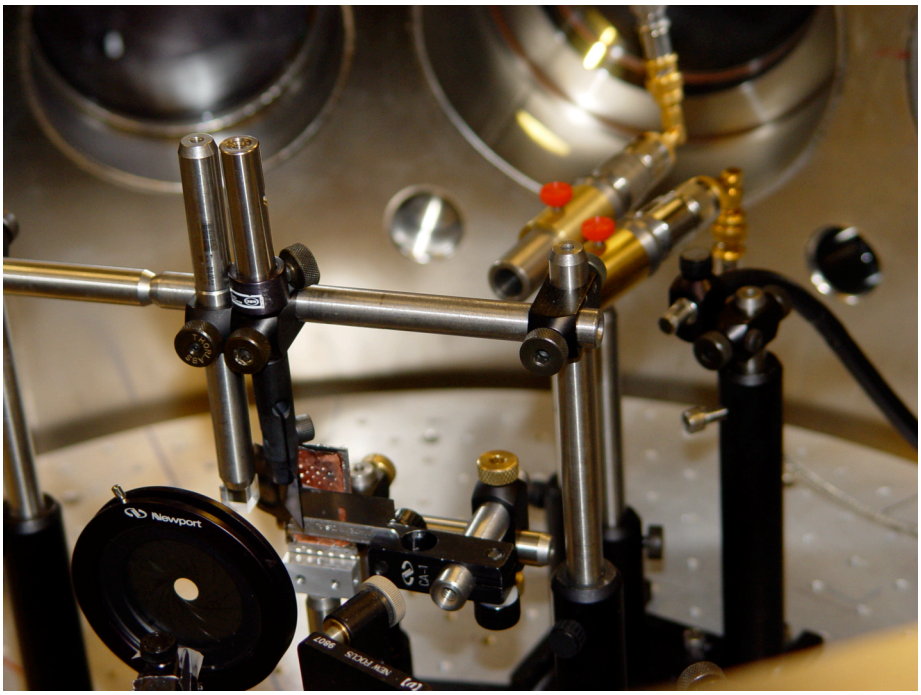

Figure 21. Closeup view from behind the Cu foil laser target . The brass housings hold Si PIN diode xray detectors.

radiation generates e-h pairs in the sensor and serves as a surrogate for xray excitation. Two AO modulators installed in series at the output of the 900 nm laser, provided ~ 8 orders of magnitude attenuation of the probe beam and were used to prepare a ~ 200 nsec duration probe pulse that overlapped the 100 fs 800 nm beam. A knife edge was passed through the 800 nm beam and CCD images were recorded. In Figure 22 we show CCD images. The left panel corresponds to a circular pump

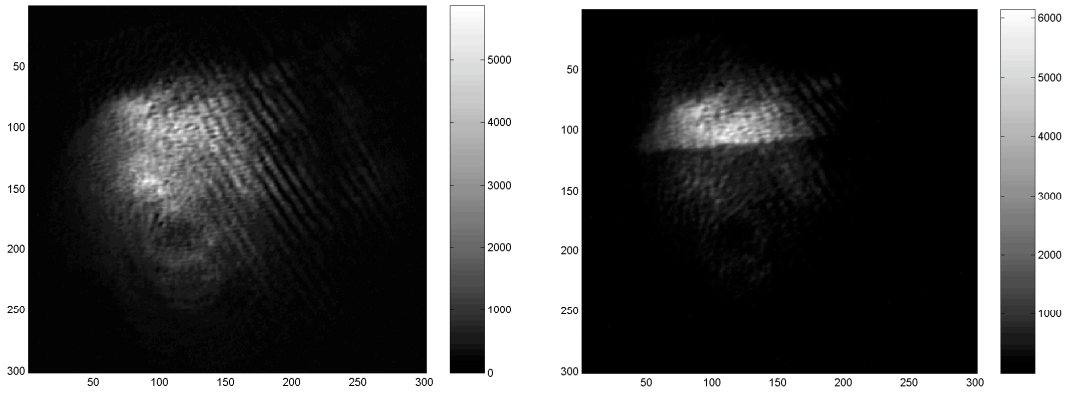

Figure 22. CCD images of the radoptic sensor transmission recorded during excitation with a 100 fs 800 nm pulse. The pump power during these measurements was ~ 10^{-6} Watts. Note that the pump acts to increase the transmission of the Fabry-Perot cavity. The left panel corresponds to no blocking of the pump. The right panel was taken with 75% obscuration of the pump beam. The units are CCD pixels, the amplitude is counts.

beam. The right panel corresponds to 75% obscuration of the pump beam. By comparing the images it is evident that the pump radiation acts to increase transmission of the cavity and the knife-edge is clearly seen in the image.

Figure 23 shows sequential images taken in the presence (right panel) and absence

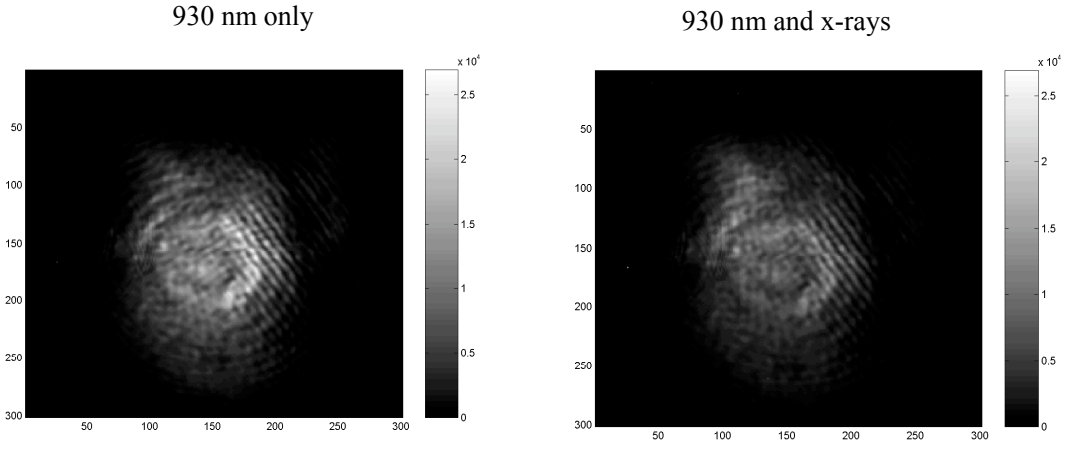

Figure 23. CCD images of the radoptic sensor transmission recorded in the presence (right panel) and absence (left panel) of xray excitation of the sensor. The sensor is biased at an operating point where xray absorption reduces the sensor transmission at 930 nm.

(left panel) of xray irradiation of the sensor. For these measurements, the sensor was biased such that xray absorption reduces the optical transmission of the sensor at 930 nm.

The effects of xray absorption are most readily discerned by subtracting the two images of Figure 23 to form the difference image illustrated in Figure 24. The

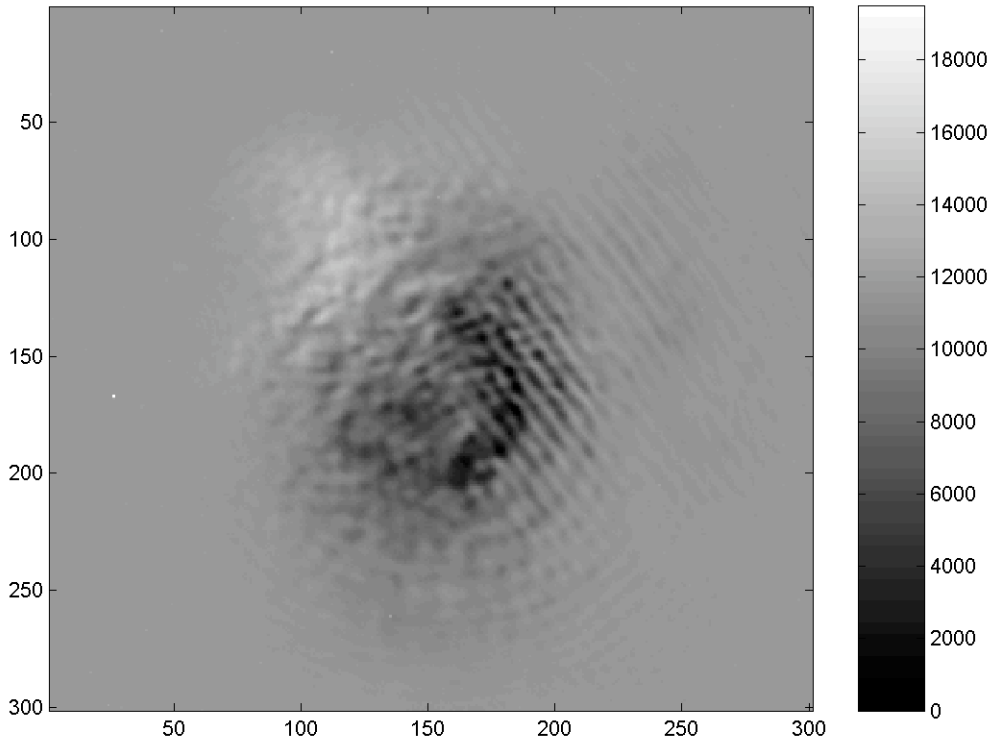

Figure 24. Difference image generated by subtracting images shown in Figure 23 above. Note that the sensor response is non-uniform; some regions exhibit enhanced optical transmission while others show reduced optical transmission; yet, there is significant contrast in the image ~ 18000 CCED counts.

difference image exhibits a detailed structure. First, note that the sensor response is non-uniform over the beam footprint; some regions show enhanced transmission, others show reduced transmission. We attribute this to both variations in the thickness of the sensor layer and spatial non-uniformities in the reflectance of the DBR mirrors. Nevertheless there is significant contrast in the image ~ 18000 counts indicating that with better control of the fabrication process, high quality, high contrast xray images can be generated with this technique.

Exit Plan

Many experiments currently being considered at NIF, especially those weapons physics experiments requiring ignition conditions, will require high sensitivity for ionizing radiation, excellent temporal resolution, and be able to operate in a harsh background environment (high EMP and high ionizing radiatin backgrounds). New instrumentation technology, including the kind of new detector technology described here will be required. As the NIF nears completion, attention and funding will soon be directed towards the development of new instrumentation technology. The current work offers a path forward in that development effort, and we expect this technology or derivatives of it will be further developed under NIF program funding and employed in instrumentation systems at NIF.

Summary

We have successfully demonstrated that the radoptic effect in semiconductors can be used for high-speed xray detection that is single-particle sensitive. Furthermore, we note that this same effect can be used to detect any particle that produces electron-hole pairs in semiconductors; thus paving the way for the development of radiation detectors for various radiation particles.

Acknowledgements (if applicable)

We would like to acknowledge the contributions of several individuals to this project. In particular, Corey Bennett, Tiziana Bond, Rebecca (Welty) Nikolic, Elaine Behymer, Holly Petersen, Adam Krey, Rick Stewart, Nobuhiko "Nobby" Kobayashi, Victor Sperry, Phil Stephan, Cathy Reinhardt, Sean Simpson, Paul Stratton, Rich Bionta, Mark McKernan, Elden Ables, Linda Ott, Steven Bond, Jay Ayers, Otto Landen, Perry Bell and John Arthur (SSRL), made critical contributions to the success of the SSRL experiments. Rick Stewart, Brian Comaskey, Corey Bennett, Phil Stephan, Bryan Moran, Paul Stratton, Jim Bonlie, Steve Maricle, Dwight Price, Al Ellis, Otto Landen and Jim Moody contributed to the success of the (USP) Europa experiments.

References

1. For an early review, see C.N. Ironside, *Ultra-fast all-optical switching*, Contemporary Physics, Vol. 34, No1, pp.1-18 (1993).
2. Elsa Garmire, *Nonlinear Optics in Semiconductors*, Physics Today, May 1994, pp. 42-48.
3. Y.H.Lee, A. Chavez-Pirson, S.W. Koch, H.M. Gibbs, S.H. Park, J.F. morhange, A.D. Jeffery, N. Peyghambarian, L. Banyai, A.C. Gossard and W. Weigmann, *Room-temperature optical nonlinearities in GaAs*, Phys. Rev. Lett. **57**, pg. 2446 (1986).
4. S.H. Park, J.F. Morhange, A.D. Jeffery,R.A. Morgan, A.Chavez-Pirson, H.M. Gibbs, S.W. Koch and N. Peyghambarian, *Measurements of room-temperature band-gap resonant optical nonlinearities of GaAs/AlGaAs multiple quantum wells and bulk GaAs*, Appl. Phys. Lett. **52**, pg. 1201 (1988).
5. H.M. Gibbs, *Optical Bistability: Controlling Light with Light*, pp.135-137, Academic Press, Orlando (1995)
6. Lowry ME, Bennett CV, Vernon SP, Bond TC, Welty R, Behymer EM, Petersen HE, Krey A, Stewart RE, Kobayashi NP, Sperry VR, Stephan PL, Reinhardt C, Simpson S, Stratton P, Bionta RM, McKernan MA, Ables E, Ott LL, Bond SW, Ayers J, Landen OL, Bell PM, *RadSensor: x-ray detection by direct modulation of an optical probe beam*, Proceedings of SPIE **5194**, pp.193-204, (2004).